

1 A Gaussian process model of human electrocorticographic  
2 data

3 Lucy L. W. Owen<sup>1</sup>, Tudor A. Muntianu<sup>1</sup>, Andrew C. Heusser<sup>1,2</sup>,  
Patrick Daly<sup>3</sup>, Katherine Scangos<sup>3</sup>, and Jeremy R. Manning<sup>1\*</sup>

<sup>1</sup>Department of Psychological and Brain Sciences, Dartmouth College,  
Hanover, NH 03755, USA

<sup>2</sup>Akili Interactive,  
Boston, MA 02110, USA

<sup>3</sup>Weill Institute for Neurosciences, University of California, San Francisco,  
San Francisco, CA 94121, USA

4 **Abstract**

5 We present a model-based method for inferring full-brain neural activity at millimeter-scale spatial  
6 resolutions and millisecond-scale temporal resolutions using standard human intracranial recordings.  
7 Our approach assumes makes the simplifying assumptions that different people's brains exhibit similar  
8 correlational structure, and that activity and correlation patterns vary smoothly over space. One can  
9 then ask, for an arbitrary individual's brain: given recordings from a limited set of locations in that  
10 individual's brain, along with the observed spatial correlations learned from other people's recordings,  
11 how much can be inferred about ongoing activity at *other* locations throughout that individual's brain?  
12 We show that our approach generalizes across people and tasks, thereby providing a person- and task-  
13 general means of inferring high spatiotemporal resolution full-brain neural dynamics from standard  
14 low-density intracranial recordings.

15 **Keywords:** Electrocorticography (ECoG), intracranial electroencephalography (iEEG), local field potential (LFP),  
16 epilepsy, maximum likelihood estimation, Gaussian process regression

18 **Introduction**

19 Modern human brain recording techniques are fraught with compromise (Sejnowski et al. 2014). Com-  
20 monly used approaches include functional magnetic resonance imaging (fMRI), scalp electroencephalog-  
21 raphy (EEG), and magnetoencephalography (MEG). For each of these techniques, neuroscientists and  
22 electrophysiologists must choose to optimize spatial resolution at the cost of temporal resolution (e.g.,  
23 as in fMRI) or temporal resolution at the cost of spatial resolution (e.g., as in EEG and MEG). A less  
24 widely used approach (due to requiring work with neurosurgical patients) is to record from electrodes  
25 implanted directly onto the cortical surface (electrocorticography; ECoG) or into deep brain structures

<sup>26</sup> (intracranial EEG; iEEG). However, these intracranial approaches also require compromise: the high  
<sup>27</sup> spatiotemporal resolution of intracranial recordings comes at the cost of substantially reduced brain  
<sup>28</sup> coverage, since safety considerations limit the number of electrodes one may implant in a given patient's  
<sup>29</sup> brain. Further, the locations of implanted electrodes are determined by clinical, rather than research,  
<sup>30</sup> needs.

<sup>31</sup> An increasingly popular approach is to improve the effective spatial resolution of MEG or scalp EEG  
<sup>32</sup> data by using a geometric approach called *beamforming* to solve the biomagnetic or bioelectrical inverse  
<sup>33</sup> problem (Sarvas 1987). This approach entails using detailed brain conductance models (often informed  
<sup>34</sup> by high spatial resolution anatomical MRI images) along with the known sensor placements (localized  
<sup>35</sup> precisely in 3D space) to reconstruct brain signals originating from theoretical point sources deep in the  
<sup>36</sup> brain (and far from the sensors). Traditional beamforming approaches must overcome two obstacles.  
<sup>37</sup> First, the inverse problem beamforming seeks to solve has infinitely many solutions. Researchers have  
<sup>38</sup> made ~~traction~~ progress towards constraining the solution space by assuming that signal-generating  
<sup>39</sup> sources are localized on a regularly spaced grid spanning the brain and that individual sources are  
<sup>40</sup> small relative to their distances to the sensors (Baillet et al. 2001; Hillebrand et al. 2005; Snyder 1991).  
<sup>41</sup> The second, and in some ways much more serious, obstacle is that the magnetic fields produced by  
<sup>42</sup> external (noise) sources are substantially stronger than those produced by the neuronal changes being  
<sup>43</sup> sought (i.e., at deep structures, as measured by sensors at the scalp). This means that obtaining adequate  
<sup>44</sup> signal quality often requires averaging the measured responses over tens to hundreds of responses or  
<sup>45</sup> trials (e.g., see review by Hillebrand et al. 2005).

<sup>46</sup> Another approach to obtaining high spatiotemporal resolution neural data has been to collect fMRI  
<sup>47</sup> and EEG data simultaneously. Simultaneous fMRI-EEG has the potential to balance the high spatial  
<sup>48</sup> resolution of fMRI with the high temporal resolution of scalp EEG, thereby, in theory, providing the  
<sup>49</sup> best of both worlds. In practice, however, the signal quality of both recordings suffers substantially  
<sup>50</sup> when the two techniques are applied simultaneously (e.g., see review by Huster et al. 2012). In addition,

51 the experimental designs that are ideally suited to each technique individually are somewhat at odds.  
52 For example, fMRI experiments often lock stimulus presentation events to the regularly spaced image  
53 acquisition time (TR), which maximizes the number of post-stimulus samples. By contrast, EEG experi-  
54 ments typically employ jittered stimulus presentation times to maximize the experimentalist's ability to  
55 distinguish electrical brain activity from external noise sources such as from 60 Hz alternating current  
56 power sources.

57 The current "gold standard" for precisely localizing signals and sampling at high temporal resolution  
58 is to take (ECoG or iEEG) recordings from implanted electrodes (but from a limited set of locations in  
59 any given brain). This begs the following question: what can we infer about the activity exhibited by the  
60 rest of a person's brain, given what we learn from the limited intracranial recordings we have from their  
61 brain and additional recordings taken from *other* people's brains? Here we develop an approach, which  
62 we call *SuperEEG*<sup>1</sup>, based on Gaussian process regression (Rasmussen 2006). SuperEEG entails using  
63 data from multiple people to estimate activity patterns at arbitrary locations in each person's brain (i.e.,  
64 independent of their electrode placements). We test our SuperEEG approach using two large datasets  
65 of intracranial recordings (Ezzyat et al. 2017, 2018; Horak et al. 2017; Kragel et al. 2017; Kucewicz et al.  
66 2017, 2018; Lin et al. 2017; Manning et al. 2011, 2012; Sederberg et al. 2003, 2007a,b; Solomon et al. 2018;  
67 Weidemann et al. 2019). We show that the SuperEEG algorithm recovers signals well from electrodes  
68 that were held out of the training dataset. We also examine the factors that influence how accurately  
69 activity may be estimated (recovered), which may have implications for electrode design and placement  
70 in neurosurgical applications.

## 71 Approach

72 The SuperEEG approach to inferring high temporal resolution full-brain activity patterns is outlined and  
73 summarized in Figure 1. We describe (in this section) and evaluate (in *Results*) our approach using ~~a~~two

<sup>1</sup>The term "SuperEEG" was coined by Robert J. Sawyer in his popular science fiction novel *The Terminal Experiment* Sawyer (1995) (Sawyer 1995). SuperEEG is a fictional technology that measures ongoing neural activity throughout the entire living human brain ~~with perfect precision and~~ at arbitrarily high spatiotemporal resolution.

<sup>74</sup> large previously collected ~~dataset~~datasets comprising multi-session intracranial recordings. Dataset 1  
<sup>75</sup> comprises multi-session recordings taken from 6876 electrodes implanted in the brains of 88 epilepsy  
<sup>76</sup> patients (Manning et al. 2011, 2012; Sederberg et al. 2003, 2007a,b). Each recording session lasted  
<sup>77</sup> from 0.2–3 h (total recording time: 0.3–14.2 h; Fig. S6E). During each recording session, the patients  
<sup>78</sup> participated in a free recall list learning task, which lasted for up to approximately 1 h. In addition,  
<sup>79</sup> the recordings included “buffer” time (the length varied by patient) before and after each experimental  
<sup>80</sup> session, during which the patients went about their regular hospital activities (confined to their hospital  
<sup>81</sup> room, and primarily in bed). These additional activities included interactions with medical staff and  
<sup>82</sup> family, watching television, reading, and other similar activities. For the purposes of the Dataset 1  
<sup>83</sup> analyses presented here, we aggregated all data across each recording session, including recordings  
<sup>84</sup> taken during the main experimental task as well as during non-experimental time. We used Dataset  
<sup>85</sup> 1 to develop our main SuperEEG approach, and to examine the extent to which SuperEEG might be  
<sup>86</sup> able to generate task-general predictions. Dataset 2 comprised multi-session recordings from ~~4436~~14860  
<sup>87</sup> electrodes implanted in the brains of ~~40~~131 epilepsy patients (Ezzyat et al. 2017, 2018; Horak et al. 2017;  
<sup>88</sup> Kragel et al. 2017; Kucewicz et al. 2017, 2018; Lin et al. 2017; Solomon et al. 2018; Weidemann et al. 2019).  
<sup>89</sup> Each recording session lasted from 0.4–2.2 h (total recording time: 0.4–6.6 h; Fig. S6K). Whereas Dataset  
<sup>90</sup> 1 included recordings taken as the patients participated in a variety of activities, Dataset 2 included  
<sup>91</sup> recordings taken as each patient performed each of two specific experimental memory tasks: a random  
<sup>92</sup> word list free recall task (Experiment 1) and a categorized word list free recall task (Experiment 2). We  
<sup>93</sup> used Dataset 2 to further examine the ability of SuperEEG to generalize its predictions within versus  
<sup>94</sup> across tasks. Figure S6 provides additional information about both datasets.

<sup>95</sup> We first applied fourth order Butterworth notch ~~filter~~filters to remove 60 Hz ( $\pm .5$  Hz) line noise  
<sup>96</sup> from every recording (from every electrode). Next, we downsampled the recordings (regardless of the  
<sup>97</sup> original samplerate) to 250 Hz. (This downsampling step served to both normalize for differences in  
<sup>98</sup> sampling rates across patients and to ease the computational burden of our subsequent analyses. )

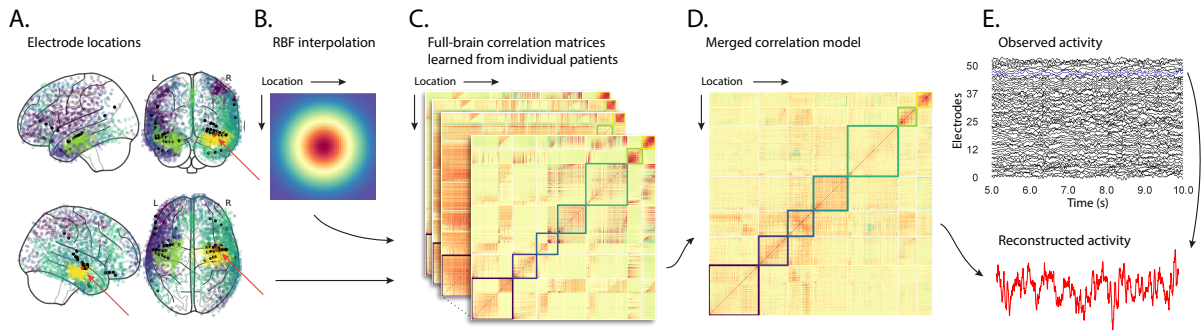


**Figure 1: Methods overview.** **A. Electrode locations.** Each dot reflects the location of a single electrode implanted in the brain of a Dataset 1 patient. A held-out recording location from one patient is indicated in red, and the patient’s remaining electrodes are indicated in black. The electrodes from the remaining patients are colored by  $k$ -means cluster (computed using the full-brain correlation model shown in Panel D). **B. Radial basis function kernel.** Each electrode contributed by the patient (black) weights on the full set of locations under consideration (all dots in Panel A, defined as  $\bar{R}\bar{R}$  in the text). The weights fall off with positional distance (in MNI<sub>152</sub> space) according to an RBF. **C. Per-patient correlation matrices.** After computing the pairwise correlations between the recordings from each patient’s electrodes, we use RBF-weighted averages to estimate correlations between all locations in  $\bar{R}\bar{R}$ . We obtain an estimated full-brain correlation matrix using each patient’s data. **D. Merged correlation model.** We combine the per-patient correlation matrices (Panel C) to obtain a single full-brain correlation model that captures information contributed by every patient. Here we have sorted the rows and columns to reflect  $k$ -means clustering labels (using  $k=7$ ; Yeo et al. 2011), whereby we grouped locations based on their correlations with the rest of the brain (i.e., rows of the matrix displayed in the panel). The boundaries denote the cluster groups. The rows and columns of Panel C have been sorted using the Panel D-derived cluster labels. **E. Reconstructing activity throughout the brain.** Given the observed recordings from the given patient (shown in black; held-out recording is shown in blue), along with a full-brain correlation model (Panel D), we use Equation 12 to reconstruct the most probable activity at the held-out location (red).

99 We then excluded any electrodes that showed putative epileptiform activity. Specifically, we excluded  
 100 from further analysis any electrode that exhibited ~~an-a~~ maximum kurtosis of 10 or greater across all  
 101 of that patient's recording sessions. We also excluded any patients with fewer than 2 electrodes that  
 102 passed this criteria, as the SuperEEG algorithm requires measuring correlations between 2 or more elec-  
 103 trodes from each patient. For Dataset 1, this yielded clean recordings from 4168 electrodes implanted  
 104 throughout the brains of 67 patients (Fig. 1A, colored dots); for Dataset 2, this yielded clean record-  
 105 ings from ~~3159 electrodes from 24~~ 5023 electrodes implanted in 78 patients. Each individual patient  
 106 ~~contributes contributed~~ electrodes from a limited set of brain locations, which we localized in a common  
 107 space (MNI152; Grabner et al. 2006); an example Dataset 1 patient's 54 electrodes that ~~passed the above~~  
 108 ~~kurtosis threshold test survived the kurtosis thresholding procedure~~ are highlighted in black and red ~~+~~  
 109 (Fig. 1A).

The recording from a given electrode is maximally informative about the activity of the neural tissue immediately surrounding its recording surface. However, brain regions that are distant from the recording surface of the electrode also contribute to the recording, albeit (*ceteris paribus*) to a much lesser extent. One mechanism underlying these contributions is volume conduction. The precise rate of falloff due to volume conduction (i.e., how much a small volume of brain tissue at location  $x$  contributes to the recording from an electrode at location  $\eta$ ) depends on the size of the recording surface, the electrode's impedance, and the conductance profile of the volume of brain between  $x$  and  $\eta$ . As an approximation of this intuition, we place a Gaussian radial basis function (RBF) at the location  $\eta$  of each electrode's recording surface (Fig. 1B). We use the values of the RBF at any brain location  $x$  as a rough estimate of how much structures around  $x$  contributed to the recording from location  $\eta$ :

$$\text{rbf}(x|\eta, \lambda) = \exp \left\{ -\frac{\|x - \eta\|^2}{\lambda} \right\}, \quad (1)$$

110 where the width variable  $\lambda$  is a parameter of the algorithm (which may in principle be set according to  
 111 location-specific tissue conductance profiles) that governs the level of spatial smoothing. In choosing  $\lambda$   
 112 for the analyses presented here, we sought to maximize spatial resolution (which implies a small value

113 of  $\lambda$ ) while also maximizing the algorithm's ability to generalize to any location throughout the brain,  
 114 including those without dense electrode coverage (which implies a large value of  $\lambda$ ). Here we set  $\lambda = 20$ ,  
 115 guided in part by our prior related work (Manning et al. 2014, 2018), and in part by examining the brain  
 116 coverage with non-zero weights achieved by placing RBFs at each electrode location in Dataset 1 and  
 117 taking the sum (across all electrodes) at each voxel in a  $4 \text{ mm}^3$  MNI brain. (We then held  $\lambda$  fixed for our  
 118 analyses of Dataset 2.) We note that this value could in theory be further optimized, e.g., using cross  
 119 validation or a formal model (e.g., Manning et al. 2018).

120 A second mechanism whereby a given region  $x$  can contribute to the recording at  $\eta$  is through (direct  
 121 or indirect) anatomical connections between structures near  $x$  and  $\eta$ . We—Although anatomical and  
 122 functional correlations can differ markedly (e.g., Adachi et al. 2012; Goñi et al. 2014; Honey et al. 2009),  
 123 we use temporal correlations in the data to estimate these anatomical connections (Becker et al. 2018).  
 124 Let  $\bar{\mathcal{R}}\bar{\mathcal{R}}$  be the set of locations at which we wish to estimate local field potentials, and let  $\mathcal{R}_s \subseteq \bar{\mathcal{R}}\bar{\mathcal{R}}_s \subseteq \bar{\mathcal{R}}$   
 125 be set of locations at which we observe local field potentials from patient  $s$  (excluding the electrodes that  
 126 did not pass the kurtosis test described above). In the analyses below we define  $\bar{\mathcal{R}} = \bigcup_{s=1}^S \mathcal{R}_s$ ,  $\bar{\mathcal{R}} = \bigcup_{s=1}^S \mathcal{R}_s$ .  
 127 We can calculate the expected inter-electrode correlation matrix for patient  $s$ , where  $C_{s,k}(i, j)$  is the  
 128 correlation between the time series of voltages for electrodes  $i$  and  $j$  from subject  $s$  during session  $k$ ,  
 129 using:

$$\bar{C}_s = r\left(\frac{1}{n}\left(\sum_{k=1}^n z(C_{s,k})\right)\right), \text{ where} \quad (2)$$

$$z(r) = \frac{\log(1+r) - \log(1-r)}{2} \text{ is the Fisher } z\text{-transformation and} \quad (3)$$

$$z^{-1}(z) = r(z) = \frac{\exp(2z) - 1}{\exp(2z) + 1} \text{ is its inverse.} \quad (4)$$

130 Next, we use Equation 1 to construct a number of to-be-estimated locations by number of patient  
 131 electrode locations weight matrix,  $W_s$ . Specifically,  $W_s$  approximates how informative the recordings at  
 132 each location in  $R_s$  are in reconstructing activity at each location in  $\bar{\mathcal{R}}\bar{\mathcal{R}}$ , where the contributions fall off

<sup>133</sup> with an RBF according to the distances between the corresponding locations:

$$W_s(i, j) = \text{rbf}(i|j, \lambda). \quad (5)$$

<sup>134</sup> Given this weight matrix,  $W_s$ , and the observed inter-electrode correlation matrix for patient  $s$ ,  $\bar{\mathcal{C}}_s$ ,  
<sup>135</sup> we can estimate the correlation matrix for all locations in  $\bar{\mathcal{R}}\bar{\mathcal{R}}$  ( $\hat{C}_s$ ; Fig. 1C) using:

$$\hat{N}_s(x, y) = \sum_{i=1}^{|R_s|} \sum_{j=1}^{i-1} W(x, i) \cdot W(y, j) \cdot z(\bar{C}_s(i, j)) \quad (6)$$

$$\hat{D}_s(x, y) = \sum_{i=1}^{|R_s|} \sum_{j=1}^{i-1} W(x, i) \cdot W(y, j). \quad (7)$$

$$\hat{C}_s = r\left(\frac{\hat{N}_s}{\hat{D}_s}\right). \quad (8)$$

After estimating the numerator ( $\hat{N}_s$ ) and denominator ( $\hat{D}_s$ ) placeholders for each  $\hat{C}_s$ , we aggregate these estimates across the  $S$  patients to obtain a single expected full-brain correlation matrix ( $\hat{K}$ ; Fig. 1D):

$$\hat{K} = r\left(\frac{\sum_{s=1}^S \hat{N}_s}{\sum_{s=1}^S \hat{D}_s}\right). \quad (9)$$

<sup>136</sup> Intuitively, the numerators capture the general structures of the patient-specific estimates of full-brain  
<sup>137</sup> correlations, and the denominators account for which locations were near the implanted electrodes in  
<sup>138</sup> each patient. To obtain  $\hat{K}$ , we compute a weighted average across the estimated patient-specific full-  
<sup>139</sup> brain correlation matrices, where patients with observed electrodes near a particular set of locations in  
<sup>140</sup>  $\hat{K}$  contribute more to the estimate.

<sup>141</sup> Having used the multi-patient data to estimate a full-brain correlation matrix at the set of locations  
<sup>142</sup> in  $\bar{\mathcal{R}}\bar{\mathcal{R}}$  that we wish to know about, we next use  $\hat{K}$  to estimate activity patterns everywhere in  $\bar{\mathcal{R}}\bar{\mathcal{R}}$ , given  
<sup>143</sup> observations at only a subset of locations in  $\bar{\mathcal{R}}\bar{\mathcal{R}}$  (Fig. 1E).

<sup>144</sup> Let  $\alpha_s$  be the set of indices of patient  $s$ 's electrode locations in  $\bar{\mathcal{R}}\bar{\mathcal{R}}$  (i.e., the locations in  $R_s$ ), and let  $\beta_s$   
<sup>145</sup> be the set of indices of all other locations in  $\bar{\mathcal{R}}\bar{\mathcal{R}}$ . In other words,  $\beta_s$  reflects the locations in  $\bar{\mathcal{R}}\bar{\mathcal{R}}$  where we

<sup>146</sup> did not observe a recording for patient  $s$  (these are the recording locations we will want to fill in using  
<sup>147</sup> SuperEEG). We can sub-divide  $\hat{K}$  as follows:

$$\hat{K}_{\beta_s, \alpha_s} = \hat{K}(\beta_s, \alpha_s), \text{ and} \quad (10)$$

$$\hat{K}_{\alpha_s, \alpha_s} = \hat{K}(\alpha_s, \alpha_s). \quad (11)$$

<sup>148</sup> Here  $\hat{K}_{\beta_s, \alpha_s}$  represents the correlations between the “unknown” activity at the locations indexed by  $\beta_s$   
<sup>149</sup> and the observed activity at the locations indexed by  $\alpha_s$ , and  $\hat{K}_{\alpha_s, \alpha_s}$  represents the correlations between  
<sup>150</sup> the observed recordings (at the locations indexed by  $\alpha_s$ ).

<sup>151</sup> Let  $Y_{s,k,\alpha_s}$  be the number-of-timepoints ( $T$ ) by  $|\alpha_s|$  matrix of (observed) voltages from the electrodes  
<sup>152</sup> in  $\alpha_s$  during session  $k$  from patient  $s$ . Then we can estimate the voltage from patient  $s$ 's  $k^{th}$  session at  
<sup>153</sup> the locations in  $\beta_s$  using Rasmussen (2006) as follows (Rasmussen 2006):

$$\hat{Y}_{s,k,\beta_s} = ((\hat{K}_{\beta_s, \alpha_s} \cdot \hat{K}_{\alpha_s, \alpha_s}^{-1}) \cdot Y_{s,k,\alpha_s}^T)^T. \quad (12)$$

<sup>154</sup> This equation is the foundation of the SuperEEG algorithm. Whereas we observe recordings only at  
<sup>155</sup> the locations indexed by  $\alpha_s$ , Equation 12 allows us to estimate the recordings at all locations indexed  
<sup>156</sup> by  $\beta_s$ , which we can define *a priori* to include any locations we wish, throughout the brain. This yields  
<sup>157</sup> estimates of the time-varying voltages at *every* location in  $\bar{\mathcal{R}}\bar{\mathcal{R}}$ , provided that we define  $\bar{\mathcal{R}}\bar{\mathcal{R}}$  in advance  
<sup>158</sup> to include the union of all of the locations in  $R_s$  and all of the locations at which we wish to estimate  
<sup>159</sup> recordings (i.e., a timeseries of voltages).

<sup>160</sup> We designed our approach to be agnostic to electrode impedances, as electrodes that do not exist  
<sup>161</sup> do not have impedances. Therefore our algorithm recovers voltages in standard deviation ( $z$ -scored)  
<sup>162</sup> units rather than attempting to recover absolute voltages. (This property reflects the fact that  $\hat{K}_{\beta_s, \alpha_s}$   
<sup>163</sup> and  $\hat{K}_{\alpha_s, \alpha_s}$  are correlation matrices rather than covariance matrices.) Also, we note that Equation 12  
<sup>164</sup> requires computing a  $T$  by  $T$  matrix, which can become computationally intractable-expensive when

165  $T$  is very large (e.g., for the patient highlighted in Dataset 1 patient with the longest recording time,  
166  $T = 12,786,750$ ; also see Fig. ??, T = 12786750S6, Panels E and K). However, because Equation 12 is time  
167 invariant, we may compute  $Y_{s,k,\beta_s}$  in a piecewise manner by filling in  $Y_{s,k,\beta_s}$  one row at a time (using the  
168 corresponding samples from  $Y_{s,k,\alpha_s}$ ).

169 The SuperEEG algorithm described above and in Figure 1 allows us to estimate, up to a constant  
170 scaling factor, local field potentials (LFPs) for each patient at all arbitrarily chosen locations in the set  
171  $\bar{R}$ , even if we did not record that patient's brain at all of those locations. We next turn to an evaluation of the  
172 accuracy of those estimates.

## 173 Results

174 We used a cross-validation approach to test the accuracy with which the SuperEEG algorithm recon-  
175 structs activity throughout the brain. For each patient in turn, we estimated full-brain correlation  
176 matrices (Eqn. 9) using data from all of the *other* patients. This step ensured that the data we were  
177 reconstructing could not also be used to estimate the between-location correlations that drove the recon-  
178 structions via Equation 12 (otherwise the analysis would be circular). For that held-out patient, we held  
179 out each electrode in turn. We used Equation 12 to reconstruct activity at the held-out electrode location,  
180 using the correlation matrix learned from all other patients' data as  $\hat{K}$ , and using activity recorded from  
181 the other electrodes from the held-out patient as  $Y_{s,k,\alpha_s}$ . (For analyses examining the stability of our  
182 estimates of  $\hat{K}$  across time and patients, see Figs. S7 and S8, respectively). We then asked: how closely  
183 did each of the SuperEEG-estimated recordings at those electrodes match the observed recordings from  
184 those electrodes (i.e., how closely did the estimated  $\hat{Y}_{s,k,\beta_s}$  match the observed  $Y_{s,k,\beta_s}$ )?

185 To illustrate our approach, we first examine an individual held-out raw LFP trace and its associated  
186 SuperEEG-derived reconstruction. Figure ??A displays the observed LFP from the red electrode in  
187 Figure 1A (blue), and its associated reconstruction (red), during the 5 s time window during one  
188 of the example patient's six recording sessions shown in Figure 1E. The two traces match closely

189 ( $r = 0.86, p < 10^{-10}$ ). Figure ??B displays a two-dimensional histogram of the actual versus reconstructed  
190 voltages for the entire 14.2 total hours of recordings from the example electrode (correlation:  $r = 0.91, p < 10^{-10}$ ).  
191 This example confirms that the SuperEEG algorithm recovers the recordings from this single electrode  
192 well. Next, we used this general approach to quantify the algorithm's performance across the full  
193 dataset.

194 **Observed and reconstructed LFP from a single electrode. A. Example LFP.** A 5 s recording from  
195 the red electrode in Figure 1A is displayed in blue, and the reconstructed LFP during the same time  
196 window is shown in red. **B. Observed versus reconstructed LFP over 14.2 hours.** The two-dimensional  
197 histogram reflects the relation between distributions of observed versus reconstructed voltages from  
198 one patient, across the 14.2 hours of recorded data collected over 6 recording sessions. The correlation  
199 reported in the panel is between the observed and reconstructed voltages. Both panels: all voltages are  
200 represented in standard deviation units (computed within session).

201 For each held-out electrode, from each held-out patient in turn, we computed the average correlation  
202 (across recording sessions) between the SuperEEG-reconstructed voltage traces and the observed voltage  
203 traces from that electrode. For this analysis we set  $\bar{R}$  to be the union of all electrode locations across  
204 all patients. This yielded a single correlation coefficient for each electrode location in  $\bar{R}$ , reflecting how  
205 well the SuperEEG algorithm was able to recover the recording at that location by incorporating data  
206 across patients (black histogram in Fig. 2A, map in Fig. 2C). The observed distribution of correlations was  
207 centered well above zero (mean:  $0.52, r = 0.51$ ;  $t$ -test comparing mean of distribution of  $z$ -transformed av-  
208 erage patient correlation coefficients to 0:  $t(66) = 25.08, p < 10^{-10}$ ), indicating that  
209 the SuperEEG algorithm recovers held-out activity patterns substantially better than random guessing.

210 As a stricter benchmark, we compared the quality of these across-participant reconstructions  
211 (i.e., computed using a correlation model learned from other patients' data) to reconstructions generated  
212 using a correlation model trained using the in-patient's data. In other words, for this within-patient  
213 benchmark analysis we estimated  $\hat{C}_s$  (Eqn. 8) for each patient in turn, using recordings from all of that

214 patient's electrodes except at the location we were reconstructing. These within-patient reconstructions  
215 serve as an estimate of how well data from all of the other electrodes from that single patient may be  
216 used to estimate held-out data from the same patient. This allows us to ask how much information about  
217 the activity at a given electrode might be inferred through (a) volume conductance or other sources of  
218 "leakage" from activity patterns measured from the patient's other electrodes and (b) across-electrode  
219 correlations learned from that single patient. As shown in Figure 2A (gray histogram), the distribution of  
220 within-patient correlations was centered well above zero (mean:  $0.32$ ;  $t$ -test comparing mean of  
221 distribution of  $z$ -transformed average patient correlation coefficients to 0:  $t(66) = 15.16, p < 10^{-10}$ ). How-  
222 ever, the across-patient correlations were substantially higher ( $t$ -test comparing average  $z$ -transformed  
223 within versus across patient electrode correlations:  $t(66) = 9.62, p < 10^{-10}$ ). This is  
224 an especially conservative test, given that the across-patient SuperEEG reconstructions exclude (from the  
225 correlation matrix estimates) all data from the patient whose data is being reconstructed. We repeated  
226 each of these analyses on a second independent dataset and found similar results (Fig. 2B, D; within  
227 versus across reconstruction accuracy:  $t(23) = 6.93, p < 10^{-5}$ ). We also replicated  
228 this result separately for each of the two experiments from Dataset 2 (Fig. S3). This overall finding,  
229 that reconstructions of held-out data using correlation models learned from *other* patient's data yield  
230 higher reconstruction accuracy than correlation models learned from the patient whose data is being  
231 reconstructed, has two important implications. First, it implies that distant electrodes provide additional  
232 predictive power to the data reconstructions beyond the information contained solely in nearby elec-  
233 trodes. (This follows from the fact that each patient's grid, strip, and depth electrodes are implanted in  
234 a unique set of locations, so for any given electrode the closest electrodes in the full dataset tend to come  
235 from the same patient.) Second, it implies that the spatial correlations learned using the SuperEEG  
236 algorithm are, to some extent, similar across people.

237 The recordings we analyzed from Dataset 1 comprised data collected as the patients performed  
238 a variety of (largely idiosyncratic) tasks throughout each day's recording session. That we observed

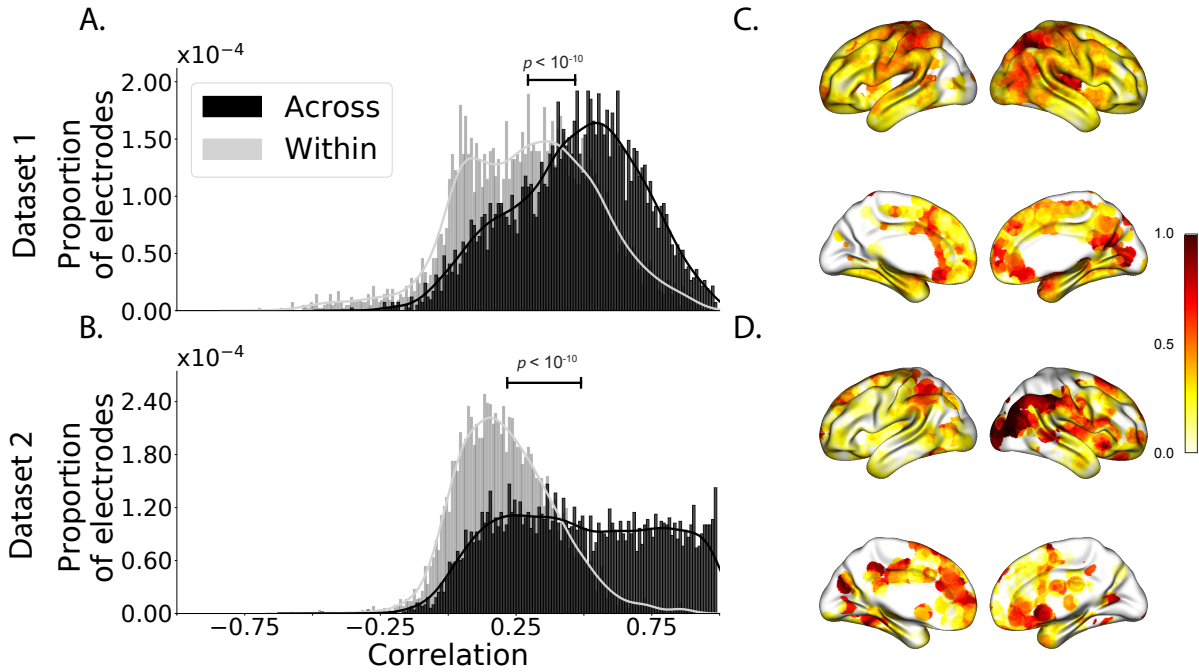


Figure 2: **Reconstruction quality across all electrodes in two ECoG datasets.** **Reconstruction accuracy across all electrodes in two ECoG datasets.** **A. Distributions of correlations between observed versus reconstructed activity by electrode, for Dataset 1.** The across-patient distribution (black) reflects reconstruction accuracy (correlation) using a correlation model learned from all but one patient's data, and then applied to that held-out patient's data. The within-patient distribution (gray) reflects performance using a correlation model learned from the same patient who contributed the to-be-reconstructed electrode. **B. Distributions of correlations for Dataset 2.** This panel is in the same format as Panel A, but reflects results obtained from Dataset 2. The histograms aggregate data across both Dataset 2 experiments; for results broken down by experiment see [Figure Figures S2 and S3](#). **C.-D. Reconstruction performance by location.** Each dot reflects the location of a single implanted electrode from Dataset 1 (Panel C) or Dataset 2 (Panel D). **C.-D. Reconstruction accuracy by location.** The dot colors denote the average across-session [correlation correlations](#), using the across-patient correlation model, between the observed and reconstructed activity at the given electrode location [projected to the cortical surface](#) (Combrisson et al. 2019). **Panel C displays the map for Dataset 1 and Panel D displays the map for Dataset 2.**

239 reliable ~~reconstruction accuracy~~ reconstructions across patients suggests that the spatial correlations  
240 derived from the SuperEEG algorithm are, to some extent, similar across tasks. We tested this finding  
241 more directly using Dataset 2. In Dataset 2, the recordings were limited to times when each patient was  
242 participating in each one of two experiments (Experiment 1 ~~is~~ a random-word list free recall task, ~~and~~  
243 Experiment 2 ~~is~~ a categorized list free recall task (24 patients participated in both)). We wondered  
244 whether a correlation model learned from data from one experiment might yield good predictions of  
245 data from the other experiment. Further, we wondered about the extent to which it might be beneficial  
246 or harmful to combine data across tasks.

247 To test the task-specificity of the SuperEEG-derived correlation models, we restricted the dataset to  
248 the 24 patients that participated in both experiments and repeated the above within- and across-patient  
249 cross validation procedures separately for Experiment 1 and Experiment 2 data from Dataset 2. We then  
250 compared the reconstruction accuracies for held-out electrodes, for models trained within versus across  
251 the two experiments, or combining across both experiments (Fig. S1). In every case we found that across-  
252 patient models trained using data from all other patients out-performed within-patient models trained on  
253 data only from the subject contributing the given electrode ( $ts(23) > 6.50, ps < 10^{-5}$ ). All reconstruction  
254 accuracies also reliably exceeded chance performance ( $ts(23) > 8.00, ps < 10^{-8}$ ). Average reconstruction  
255 accuracy was highest for the across-patient models limited to data from the same experiment (mean  
256 accuracy: ~~0.68~~  $r = 0.68$ ); next-highest for the models that combined data across both experiments (mean  
257 accuracy: ~~0.61~~  $r = 0.61$ ); and lowest for models trained across tasks (mean accuracy: ~~0.47~~  $r = 0.47$ ). This  
258 ~~result pattern of results~~ also held for each of the Dataset 2 experiments individually (Fig. S2). Taken  
259 together, these results indicate that there are reliable commonalities in the spatial correlations of full-brain  
260 activity across tasks, but that there are also reliable differences in these spatial correlations across tasks.  
261 Whereas reconstruction accuracy benefits from incorporating data from other patients, reconstruction  
262 accuracy is highest when constrained to within-task data, or data that includes a variety of tasks (e.g.,  
263 Dataset 1, or combining across the two Dataset 2 experiments).

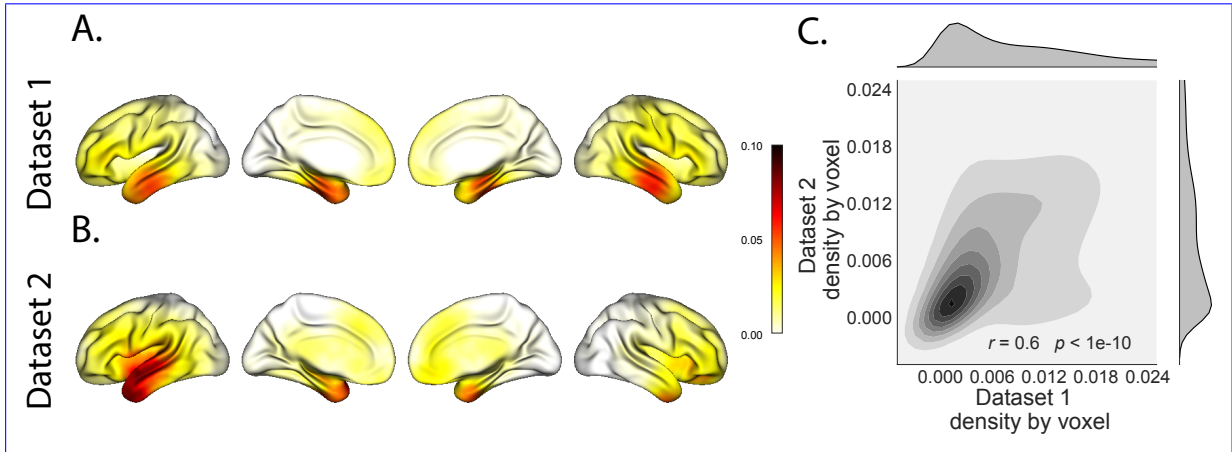


Figure 3: **Electrode sampling density by location.** **A.** **Electrode sampling density by voxel location in Dataset 1.** Each voxel is colored by the proportion of total electrodes in the dataset that are located within 20 MNI units of the given voxel. **B.** **Electrode sampling density by voxel location in Dataset 2.** This panel displays the sampling density map for Dataset 2, in the same format as Panel A. **C.** **Correspondence in sampling density by voxel location across Datasets 1 and 2.** The two-dimensional histogram displays the per-voxel sampling densities in the two Datasets, and the one-dimensional histograms display the proportions of voxels in each dataset with the given density value. The correlation reported in the panel is across voxels in the  $4 \text{ mm}^3$  MNI152 brain.

Although both datasets we examined provide good full-brain coverage (when considering data from every patient; e.g., Fig. 2C, D), electrodes are not placed uniformly throughout the brain. For example, in our patient population, electrodes are more likely to be implanted in regions like the medial temporal lobe (MTL), and are rarely implanted in occipital cortex (Fig. 3A, B). Separately for each dataset, for each voxel in the  $4 \text{ mm}^3$  voxel MNI152 brain, we computed the proportion of electrodes in the dataset that were contained within a 20 MNI unit radius sphere centered on that voxel. We defined the *density* at that location as this proportion. Across Datasets 1 and 2, the electrode placement densities were similar (correlation by voxel:  $r = -0.56, p < 10^{-10}$   $r = 0.6, p < 10^{-10}$ ). We wondered whether regions with good coverage might be associated with better reconstruction accuracy (e.g., For example, Figures 2C and D indicate that many some electrodes in the MTL (which tends to be densely sampled) have relatively high reconstruction accuracy, and occipital electrodes (which tends to be relatively sparsely sampled) tend to have relatively low reconstruction accuracy). To test whether this held more generally across the entire brain, for each dataset we computed the electrode placement

density for each electrode from each patient (using the proportion of *other* patients' electrodes within 20 MNI units of the given electrode). We then correlated these density values with the across-patient reconstruction accuracies for each electrode. We found no reliable ~~correlations~~ correlation between reconstruction accuracy and density for either dataset (Dataset 1:  $r = 0.09, p = 0.44$ ; ( $r = 0.05, p = 0.70$ ) and a reliable negative correlation for Dataset 2:  $r = -0.30, p = 0.15$  ( $r = -0.21, p = 0.05$ ). This indicates suggests that the reconstruction accuracies we observed are ~~not~~ not driven solely by sampling density, but rather may also reflect higher order properties of neural dynamics such as functional correlations between distant voxels (Betzel et al. 2017).

Prior work in humans and animals has shown that the spatial profile of the local field potential differs by frequency band (e.g., with respect to volume conductance properties and contribution to the local field potential; Buzsaki et al. 2014). For example, lower frequency components of the local field potential tend to have higher power and extend further in space than high-frequency components (e.g., Manning et al. 2009; Miller et al. 2007). We wondered whether the reconstructions we observed might be differently weighting or considering the contributions of activity at different frequency bands. We therefore examined a range of frequency bands ( $\delta$ : 2–4 Hz;  $\theta$ : 4–8 Hz;  $\alpha$ : 8–12 Hz;  $\beta$ : 12–30 Hz;  $\gamma_L$ : 30–60 Hz; and  $\gamma_H$ : 60–100 Hz), along with a measure of broadband (BB) power. We used second-order Butterworth bandpass filters to compute the activity patterns within each narrow frequency band. We defined broadband power as the mean height of a linear robust regression fit in log-log space to the order 4 Morlet wavelet-computed power spectrum at 50 log-spaced frequencies from 2–100 Hz (Manning et al. 2009). We then repeated our within-subject and across-subject cross-validated reconstruction accuracy tests (analogous to Fig. 2) separately for each frequency band (Fig. 4). (We also carried out a similar analysis on the Hilbert transform-computed spectral power within each narrow band; see Fig. S4.) Across both datasets, we found that our approach is best at reconstructing patterns of broadband activity (right-most bars in Figs. 4A and D), a correlate of population firing rate (Manning et al. 2009). We also achieved good reconstruction accuracy within each narrow frequency band (Figs. 4 and S4). Activity at lower frequencies ( $\delta$ ,  $\theta$ ,  $\alpha$ , and  $\beta$ ) tended to be

302 reconstructed better than high-frequency patterns ( $\gamma_L$  and  $\gamma_H$ ), with reconstruction accuracy peaking in  
303 the  $\theta$  band. Overall, these results indicate that our approach is able to accurately recover information  
304 within the 2–100 Hz range.

305 In neurosurgical applications where one wishes to infer full-brain activity patterns, can our framework  
306 yield insights into where the electrodes should be placed? A basic assumption of our approach (and of  
307 most prior ECoG work) is that electrode recordings are most informative about the neural activity near  
308 the recording surface of the electrode. But if we consider that activity patterns throughout the brain are  
309 meaningfully correlated, are there particular implantation locations that, if present in a recorded from  
310 a given patient's brain, yield especially high reconstruction accuracies throughout the rest of the their  
311 brain? For example, one might hypothesize that brain structures that are heavily interconnected with  
312 many other structures could be more informative about full-brain activity patterns than comparatively  
313 isolated structures.

314 To gain insights into whether particular electrode locations might be especially informative, we first  
315 To test this hypothesis, we computed the average reconstruction accuracy across all of each patient's  
316 electrodes (using the our across-patients cross validation test; black histograms in Fig. 2A and B). We  
317 first labeled each patient's electrodes, in each dataset, with the average reconstruction accuracy for that  
318 patient. In other words, we assigned every electrode from each given patient the same value, reflecting  
319 how well the activity patterns at those electrodes were reconstructed on average for that patient were  
320 reconstructed. Next, for each voxel in the 4 mm<sup>3</sup> MNI brain, we computed the average value across  
321 any electrode (from any patient) that came within 20 MNI units of that voxel's center. Effectively, we  
322 computed This yielded an information score for each voxel, reflecting the (weighted) average reconstruction  
323 accuracy across any patients with electrodes near each voxel voxel, where the averages were weighted to  
324 reflect patients who had more electrodes implanted near that location. This yielded We created a single  
325 map of these information scores for each dataset, highlighting regions that are potentially promising  
326 implantation targets in terms of providing full-brain activity information via SuperEEG (Fig especially

**Electrode sampling density by location.** **A. Electrode sampling density by voxel in Dataset 1.** Each voxel is colored by the proportion of total electrodes in the dataset that are located within a 20 MN1 unit radius sphere centered on the given voxel. **B. Electrode sampling density by voxel in Dataset 2.** This panel displays the sampling density map for Dataset 2, in the same format as Panel A. **C. Correspondence in sampling density by voxel across Datasets 1 and 2.** The two-dimensional histogram displays the by-voxel densities in the two Datasets, and the one-dimensional histograms display the proportions of voxels in each dataset with the given density value. The correlation reported in the panel is across voxels in the 4 mm<sup>3</sup> MN1 brain.

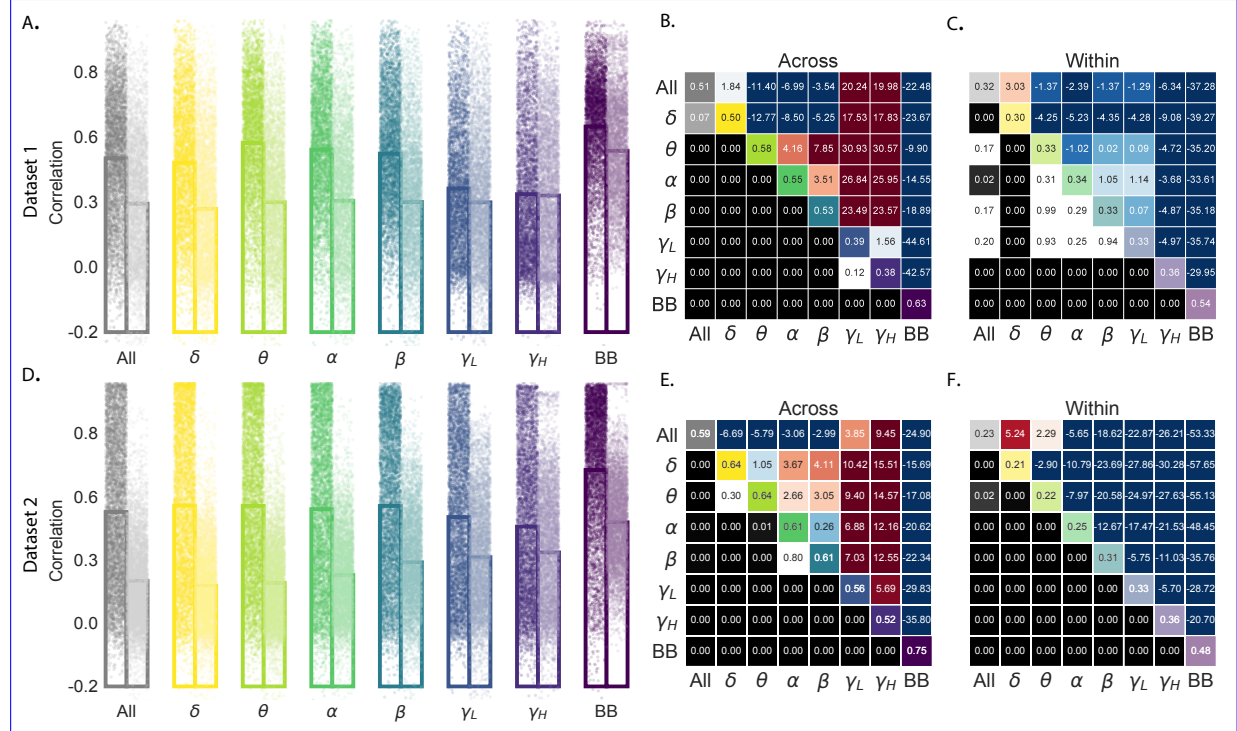


Figure 4: **Reconstruction accuracy across all electrodes in two ECoG datasets for each frequency band.** **A. Distributions of correlations between observed versus reconstructed activity by electrode for each frequency band in Dataset 1.** Each color denotes a different frequency band. Within each color group, the darker dots and bar on the left display the distribution (and mean) across-patient reconstruction accuracies (analogous to the black histograms in Fig. 2). The lighter dots and bar on the right display the distribution (and mean) within-patient reconstruction accuracies (analogous to the gray histograms in Fig. 2). Each dot indicates the reconstruction accuracy for one electrode in the dataset. To facilitate visual comparison with the frequency-specific results, the leftmost bars (gray) re-plot the histograms in Figure 2A. **B. Statistical summary of across-patient reconstruction accuracy by electrode for each frequency band in Dataset 1.** In the upper triangles of each map, warmer colors (positive  $t$ -values) indicate that the reconstruction accuracy for the frequency band in the given row was greater (via a two-tailed paired-sample  $t$ -test) than for the frequency band in the given column. Cooler colors (negative  $t$ -values) indicate that reconstruction accuracy for the frequency band in the given row was lower than for the frequency band in the given column. The lower triangles of each map denote the corresponding  $p$ -values for the  $t$ -tests. The diagonal entries display the average reconstruction accuracy within each frequency band. **C. Statistical summary of within-patient reconstruction accuracy by electrode for each frequency band in Dataset 1.** This panel displays the within-patient statistical summary, in the same format as Panel B. **D. Distributions of correlations between observed versus reconstructed activity by electrode, for each frequency band in Dataset 2.** This panel displays reconstruction accuracy distributions for each frequency band for Dataset 2. **E-F. Statistical summaries of across-patient and within-patient reconstruction accuracy by electrode for each frequency band in Dataset 2.** These panels are in the same as Panels B and C, but display results from Dataset 2.

327 informative about activity in *other* brain areas (Figs. 5A ~~and~~ B). Despite task and patient differences across  
328 the two datasets, we nonetheless found that the ~~maps of the most promising implantation targets derived~~  
329 ~~information score maps~~ from both datasets were ~~similar correlated~~ (voxelwise correlation between in-  
330 formation scores across the two datasets:  $r = 0.20, p < 10^{-10}$ ). ~~While the correspondence between the~~  
331 ~~two maps was imperfect, our~~  $r = 0.18, p < 10^{-10}$ . Our finding that there were some commonalities  
332 between the two ~~datasets' information score~~ maps lends support to the notion that different brain areas  
333 are ~~(reliably)~~ differently informative about full-brain activity patterns. We also examined the intersec-  
334 tion between the top 10% most informative voxels across the two datasets (~~white outlines gray areas~~  
335 in Fig. 5A, B, C, networks shown in Fig. 6A, top row). Supporting the notion that structures that are  
336 highly interconnected with the rest of the brain ~~might be especially good targets for implantation, this~~  
337 ~~are most informative about full-brain activity patterns, the~~ intersecting set of voxels with the highest  
338 information scores included major portions of the dorsal attention network (e.g., inferior parietal lobule,  
339 precuneus, inferior temporal gyrus, thalamus, and striatum) as well as some portions of the default  
340 mode network (e.g., angular gyrus) that are highly interconnected with a large proportion of the brain's  
341 gray matter (e.g., Tomasi and Volkow 2011)(e.g., Tomasi and Volkow 2011).

342 We also wondered whether the map of information scores might vary as a function of the spectral  
343 components of the activity patterns under consideration. We computed analogous maps of information  
344 scores for each individual frequency band. Across Datasets 1 and 2 (with the exception of  $\alpha$ -band  
345 activity), we observed reliable positive correlations between the voxelwise maps of information scores  
346 ( $\delta$ :  $r = 0.09, p < 10^{-57}$ ;  $\theta$ :  $r = 0.24, p < 10^{-60}$ ;  $\alpha$ :  $r = -0.03, p < 0.001$ ;  $\beta$ :  $r = 0.02, p = 0.0011$ ;  $\gamma_L$ :  
347  $r = 0.1, p < 10^{-67}$ ;  $\gamma_H$ :  $r = 0.03, p < 10^{-7}$ ; broadband:  $r = 0.21, p < 10^{-297}$ ).

348 To gain additional insight into which regions were most informative about full-brain activity patterns  
349 at different frequency bands, we next computed (for each frequency band) the intersection of the top  
350 10% highest information scores across the maps for Datasets 1 and 2 (analogous to our approach in  
351 Fig. 5C). This yielded a single map of the (reliably) most informative locations, for each frequency band

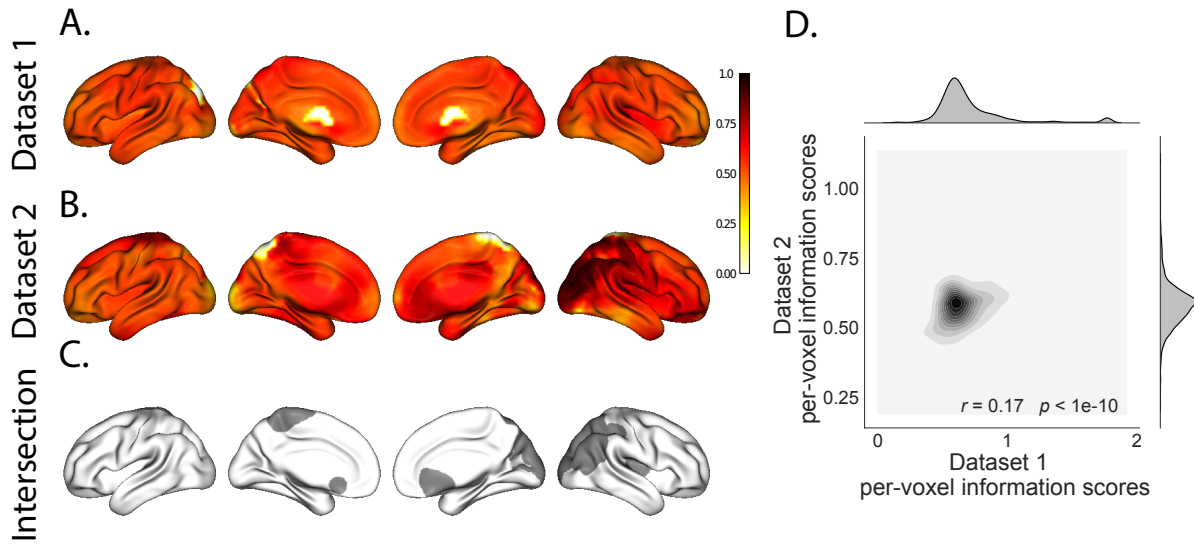


Figure 5: **Most informative electrode locations.** **A. Dataset 1 information score by voxel.** **Most informative recording locations.** **A. Dataset 1 information scores by voxel.** The voxel colors reflect the weighted average reconstruction accuracy across all electrodes from any patients with at least one electrode within 20 MNI units of the given voxel. **B. Dataset 2 information score by voxel.** **B. Dataset 2 information scores by voxel.** This panel is in the same format as Panel A. **In both panels the contours C. Intersection.** Gray areas indicate the intersections between the top 10% most informative voxels in each map (also see Fig. and projected onto the cortical surface )(Combrisson et al. 2019). **C. Correspondence in information scores by voxel across Datasets 1 and 2.** Same format as Figure 3C. **D. Correspondence in information scores by voxel across Datasets 1 and 2.** The correlation reported in the Panel is between the per-voxel information scores across Datasets 1 and 2.

352 we examined. We then carried out *post hoc* analyses on each of these maps to characterize the underlying  
353 structural and functional properties of each set of regions we identified as being particularly informative  
354 about one or more types of neural pattern (Figs. 6 and S5).

355 A growing body of neuroscientific research is concerned with characterizing the *parcellations* of  
356 anatomical and functional brain networks (for review see Arslan et al. 2018; Zalesky et al. 2010). The  
357 dominant approaches entail obtaining a full-brain connectivity matrix using either diffusion tensor  
358 imaging to identify the brain's network of white matter connections, or functional connectivity (typically  
359 applied to resting state data) to correlate the patterns of activity exhibited by different brain structures.  
360 One can then apply graph theoretic approaches to assign each brain structure (typically a single fMRI  
361 voxel) to one or more networks (for review see Bullmore and Sporns 2009). The result is a set of distinct  
362 (or partially overlapping) brain "networks" that may be further examined to elucidate their potential  
363 functional role. We overlaid a well-cited seven-network parcellation map identified by Yeo et al. (2011)  
364 onto the maps of brain locations that were most informative about each type of neural pattern. For each  
365 of these information maps, we computed the proportion of voxels in the most informative brain regions  
366 that belonged to each of the seven networks identified by Yeo et al. (2011); Figure 6D. We found that the  
367 regions we identified as being most informative about different neural patterns varied markedly with  
368 respect to which functional networks they belonged to (Fig. 6A, B).

369 The variability we observed in the frequency-specific information score maps is consistent with the  
370 notion that there is no "universal" brain region that reflects all types of activity patterns throughout the  
371 rest of the brain. Rather, each region's activity patterns appear to be characterized by different spectral  
372 profiles, and the ability to infer full-brain activity patterns at a particular frequency band depends on  
373 the structural and functional connectome specific to that frequency band (Fig. 6E). We wondered how  
374 the maps we found might fit in with prior work. To this end, in addition to examining the anatomical  
375 profiles of each map, we used Neurosynth (Rubin et al. 2017) to identify (using meta analyses of the  
376 neuroimaging literature) the top five most common terms associated with each frequency-specific map

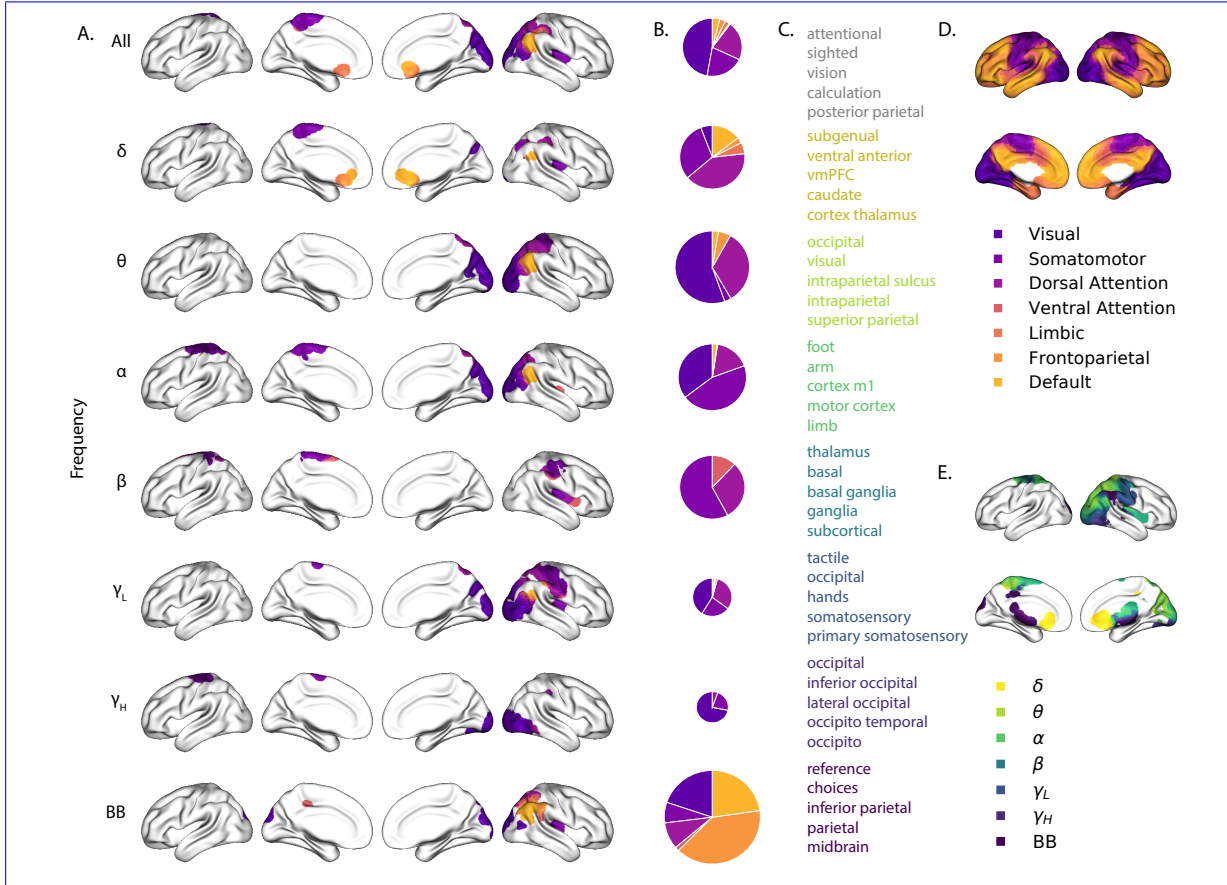


Figure 6: **Most informative recording locations by frequency band.** **A. Intersections between information score maps by frequency band.** The regions indicated in each row depict the intersection between the top 10% most informative locations across Datasets 1 and 2. **B. Network memberships of the most informative brain regions.** The pie charts display the proportions of voxels in each region that belong to the seven networks identified by Yeo et al. (2011). The relative sizes of the charts for each frequency band reflect the average across-subject reconstruction accuracies (Figs. 4A, D). The voxels in Panel A are colored according to the same network memberships. **C. Neurosynth terms associated with the most informative brain regions, by frequency band.** The lists in each row display the top five neurosynth terms (Rubin et al. 2017) decoded for each region. **D. Network parcellation map and legend.** The parcellation defined by Yeo et al. (2011) is displayed on the inflated brain maps. The colors and network labels serve as a legend for Panels A and B. **E. Combined map of the most informative brain regions.** The map displays the union of the most informative maps in Panel A, colored by frequency band. The labels also serve as a legend for Panel C.

377 (Fig. 6C). We found that  $\delta$  patterns across the brain were best predicted by regions of ventromedial  
378 prefrontal cortex, striatum, and thalamus (yellow). These regions are also implicated in modulating  
379  $\delta$  oscillations during sleep, and are heavily interconnected with cortex (e.g., Amzica and Steriade 1998)  
380 . The brain areas most informative about full-brain  $\theta$  patterns were occipital and parietal regions  
381 associated with visual processing and visual attention (light green). Prior work has implicated  $\theta$   
382 oscillations in these areas in periodic sampling of visual attention (e.g., Busch and VanRullen 2010). We  
383 found that full-brain  $\alpha$  patterns were best predicted by motor areas (dark green), which also exhibit  
384  $\alpha$  band changes during voluntary movements (e.g., Jurkiewicz et al. 2006). Striatum and thalamus  
385 (teal) were most informative about full-brain  $\beta$  patterns. Prior work has implicated striatal  $\beta$  activity  
386 in sensory and motor processing (Feingold et al. 2015) and thalamic  $\beta$  activity has been implicated in  
387 modulating widespread  $\beta$  patterns across neocortex (Sherman et al. 2016). Somatosensory areas (dark  
388 blue) were most informative about full-brain  $\gamma_L$  patterns. Prior work has implicated somatosensory  $\gamma_L$   
389 in somatosensory processing and motor planning (Ihara et al. 2003). Occipital cortex (purple) was most  
390 informative about full-brain  $\gamma_H$  patterns. Occipital  $\gamma_H$  has also been linked with visual processing and  
391 reading (Wu et al. 2011) and the transmission of visual representations from low-order to higher-order  
392 visual areas (Matsumoto et al. 2013). Full-brain broadband patterns were best predicted by inferior  
393 parietal cortex precuneus (maroon). Functional neuroimaging BOLD responses (Simony et al. 2016)  
394 and broadband ECoG patterns (Honey et al. 2012) in these default-mode hubs have been implicated in  
395 processing context-dependent representations that unfold over long timescales.

396 Taken together, the frequency-specific information maps suggest a potential new interpretation  
397 of many of the above previously reported findings. Prior work has largely treated region-specific  
398 narrowband and broadband activity as an indicator that activity at those frequency ranges reflects that  
399 the given region is representing or supporting a particular function. Our work suggests an alternative  
400 interpretation that when we observe a particular neural pattern in a particular brain region, it may  
401 instead reflect how that region is transmitting information to the rest of the brain via signalling at the

402 given frequency range.

403 **Discussion**

404 Are our brain's networks static or dynamic? And to what extent are the network properties of our brains  
405 stable across people and tasks? One body of work suggests that our brain's *functional* networks are dy-  
406 namic (e.g., Manning et al. 2018) (e.g., Manning et al. 2018; Owen et al. 2019), person-specific (e.g., Finn  
407 et al. 2015), and task-specific (e.g., Turk-Browne 2013). In contrast, although the gross anatomical struc-  
408 ture of our brains changes meaningfully over the course of years as our brains develop, on the timescales  
409 of typical neuroimaging experiments (i.e., hours to days) our anatomical networks are largely stable (e.g.,  
410 Casey et al. 2000). Further, many aspects of brain anatomy, including white matter structure, are largely  
411 preserved across people (e.g., Jahanshad et al. 2013; Mori et al. 2008; Talairach and Tournoux 1988).  
412 There are several possible means of reconciling this apparent inconsistency between dynamic person-  
413 and task-specific functional networks versus stable anatomical networks. For example, relatively small  
414 magnitude anatomical differences across people may be reflected in reliable functional connectivity dif-  
415 ferences. Along these lines, one recent study found that diffusion tensor imaging (DTI) structural data  
416 is similar across people, but may be used to predict person-specific resting state functional connectivity  
417 data (Becker et al. 2018). Similarly, other work indicates that task-specific functional connectivity may  
418 be predicted by resting state functional connectivity data (Cole et al. 2016; Tavor et al. 2016). Another  
419 (potentially complementary) possibility is that our functional networks are constrained by anatomy, but  
420 nevertheless exhibit (potentially rapid) task-dependent changes (e.g., Sporns and Betzel 2016).

421 Here we have taken a model-based approach to studying whether high spatiotemporal resolution  
422 activity patterns throughout the human brain may be explained by a static connectome model that is  
423 shared across people and tasks. Specifically, we trained a model to take in recordings from a subset  
424 of brain locations, and then predicted activity patterns during the same interval, but at *other* loca-  
425 tions that were held out from the model. Our model, based on Gaussian process regression, was

426 built on three general hypotheses about the nature of the correlational structure of neural activity  
427 (each of which we tested). First, we hypothesized that functional correlations are stable over time  
428 and across tasks. We found that, although aspects of the patients' functional correlations were sta-  
429 ble across tasks, we achieved better reconstruction accuracy when we trained the model on within-task  
430 data (we acknowledge that our general approach could potentially be extended to better model across-task changes, follow  
431 This suggests that our general approach could be extended to better model across-task changes, e.g.,  
432 following Cole et al. (2016); Tavor et al. (2016); and others. Second, we hypothesized that some of the  
433 correlational structure of people's brain activity is similar across individuals. Consistent with this hy-  
434 pothesis, our model explained the each patient's data best when we trained the correlation model trained  
435 using data from *other* patients— even when compared to a correlation model trained on the same patient's  
436 data models trained within-patient. Third, we resolved ambiguities in the data by hypothesizing that  
437 neural activity from nearby sources will tend tends to be similar, all else being equal. This hypothesis  
438 was supported through our finding that all of the models we trained that incorporated this spatial  
439 smoothness assumption predicted held-out data well above chance.

440 One potential limitation of our approach is that it does not provide a natural means of estimating  
441 the precise timing of single-neuron action potentials. Prior work has shown that gamma band and  
442 broadband activity in the LFP may be used to estimate the firing rates of neurons that underly the  
443 population contributing to the LFP (Crone et al. 2011; Jacobs et al. 2010; Manning et al. 2009; Miller et al.  
444 2008). Because SuperEEG reconstructs LFPs throughout the brain, one could in principle use gamma or  
445 broadband power in the reconstructed signals to estimate the corresponding firing rates (though not the  
446 timings of individual action potentials). We found that we were able to reconstruct full-brain patterns  
447 of broadband power well (Fig. 4).

448 A second potential limitation of our approach is that it relies on ECoG data from epilepsy patients.  
449 Recent work comparing functional correlations in epilepsy patients (measured using ECoG) and healthy  
450 individuals (measured using fMRI) suggests that there are gross similarities between these populations (e.g., Kucyi et al. 2011)

451 Nevertheless, because all of the patients we examined have drug-resistant epilepsy, it remains uncertain  
452 how generally the findings reported here might apply more broadly to the population at large (e.g.,  
453 non-clinical populations).

454 Beyond providing a means of estimating ongoing activity throughout the brain using already  
455 implanted already-implanted electrodes, our work also has implications for where to place the electrodes  
456 in the first place how to optimize electrode placements in neurosurgical evaluations. Electrodes are typi-  
457 cally implanted to maximize coverage of suspected epileptogenic tissue. However, our findings suggest  
458 that this approach could be further optimized might be improved upon. Specifically, one could leverage  
459 not only the non-invasive recordings taken during an initial monitoring period (as is currently done  
460 routinely), but also recordings collected from other other patients. We could then ask: given what we  
461 learn from other patients' data (and potentially from the scalp EEG recordings of this new patient),  
462 where should we place a fixed number of electrodes to maximize our ability to map seizure foci? As  
463 shown in Figures 5 and 6, recordings from different locations are differently informative in  
464 terms of reconstructing the spatiotemporal activity patterns throughout the brain. This property might  
465 be leveraged in decisions about where to surgically implant electrodes in future patients regions vary  
466 with respect to how informative they are about different narrowband and broadband full-brain activity  
467 patterns.

468 By providing a means of reconstructing full-brain activity patterns, the SuperEEG approach maps  
469 ECoG recordings from different patients into a common neural space, despite that different patients'  
470 electrodes were implanted in different locations. This feature of our approach enables across-patient  
471 ECoG studies, analogous to across-subject fMRI studies (e.g., Haxby et al. 2001, 2011; Norman et al. 2006)  
472 Whereas the focus of this manuscript is to specifically evaluate which aspects of neural activity  
473 patterns SuperEEG recovers well (or poorly), in parallel work we are training across-patient classifiers  
474 by leveraging the common neural spaces obtained by applying SuperEEG to multi-patient ECoG data.  
475 For example, we have shown that SuperEEG-derived activity patterns may be used to accurately predict

476 psychiatric conditions such as depression (Scangos et al. 2020). Analogous approaches could in principle  
477 be used to develop improved brain-computer interfaces and/or to carry out other analyses that would  
478 benefit from high spatiotemporal resolution full-brain data in individuals, projected into a common  
479 ECoG space across people.

## 480 Concluding remarks

481 Over the past several decades, neuroscientists have begun to leverage the strikingly profound mathemati-  
482 cal structure underlying the brain's complexity to infer how our brains carry out computations to support  
483 our thoughts, actions, and physiological processes. Whereas traditional beamforming techniques rely on  
484 geometric source-localization of signals measured at the scalp, here we propose an alternative approach  
485 that leverages the rich correlational structure of two large datasets of human intracranial recordings. In  
486 doing so, we are one step closer to observing, and perhaps someday understanding, the full spatiotem-  
487 poral structure of human neural activity.

## 488 Code availability

489 We have published an open-source toolbox implementing the SuperEEG algorithm. It may be down-  
490 loaded [here](#). Additionally, we have provided code for all analyses and figures reported in the current  
491 manuscript, available [here](#).

## 492 Data availability

493 The ~~dataset~~ datasets analyzed in this study ~~was~~ were generously shared by Michael J. Kahana. A portion  
494 of Dataset 1 may be downloaded [here](#). Dataset 2 may be downloaded [here](#).

## 495 Acknowledgements

496 We are grateful for useful discussions with Luke J. Chang, Uri Hasson, Josh Jacobs, Michael J. Kahana,  
497 and Matthijs van der Meer. We are also grateful to Michael J. Kahana for generously sharing the ECoG

498 data we analyzed in our paper, which was collected under NIMH grant MH55687 and DARPA RAM  
499 Cooperative Agreement N66001-14-2-4-032, both to M.J.K. Our work was also supported in part by NSF  
500 EPSCoR Award Number 1632738 and by a sub-award of DARPA RAM Cooperative Agreement N66001-  
501 14-2-4-032 to J.R.M. The content is solely the responsibility of the authors and does not necessarily  
502 represent the official views of our supporting organizations.

## 503 **Author Contributions**

504 J.R.M conceived and initiated the project. L.L.W.O., T.A.M. and A.C.H. performed the analyses using  
505 software packages that all authors contributed to. J.R.M. and L.L.W.O. wrote the manuscript with input  
506 from all other authors.

## 507 **Author Information**

508 ~~Reprints and permissions information is available at [www.nature.com/reprints](http://www.nature.com/reprints). The authors declare~~  
509 ~~no competing financial interests. Readers are welcome to comment on the online version of the paper.~~  
510 ~~Publisher's note: Springer Nature remains neutral with regard to jurisdictional claims in published maps~~  
511 ~~and institutional affiliations. Correspondence and requests for materials should be addressed to J.R.M.~~  
512 ~~(jeremy.r.manning@dartmouth.edu).~~

## 513 **References**

- 514 Adachi Y, Osada T, Sporns O, Watanabe T, Matsui T, Miyamoto K, Miyashita Y 2012. Functional con-  
515 nectivity between anatomically unconnected areas is shaped by collective network-level effects in the  
516 macaque cortex. *Cerebral Cortex* 22:1586–1592.
- 517 Amzica F, Steriade M 1998. Electrophysiological correlates of sleep delta waves. *Electroencephalography*  
518 and Clinical Neurophysiology

- 519 Arslan S, Ktena S I, Makropoulos A, Robinson E C, Rueckert D, Parisot S 2018. Human brain mapping: a  
520 systematic comparison of parcellation methods for the human cerebral cortex. *NeuroImage* 170:5–30.
- 521 Baillet S, Mosher J C, Leahy R M 2001. Electromagnetic brain mapping. *IEEE Signal Processing Magazine*  
522 18:14–30.
- 523 Becker C O, Pequito S, Pappas G J, Miller M B, adn D S Bassett S T Grafton, Preciado V M  
524 2018. Spectral mapping of brain functional connectivity from diffusion imaging. *Scientific Reports*  
525 8: <https://doi.org/10.1038/s41598-017-18769-x>.
- 526 Betzel R F, Medaglia J D, Kahn A E, Soffer J, Schonhaut D R, Bassett D S 2017. Inter-regional ECoG  
527 correlations predicted by communication dynamics, geometry, and correlated gene expression. *arXiv*  
528 1706.06088.
- 529 Bullmore E., Sporns O. 2009. Complex brain networks: graph theoretical analysis of structural and  
530 functional systems. *Nature Reviews Neuroscience* 10:186–198.
- 531 Busch N A, VanRullen R 2010. Spontaneous EEG oscillations reveal periodic sampling of visual attention.  
532 *Proceedings of the National Academy of Science USA* 107:16048–16053.
- 533 Buzsaki G., Anastassiou C., Koch C. 2012. The origin of extracellular fields and currents - eeg, ecog, lfp  
534 and spikes. *Nature Reviews Neuroscience* 13:407–419.
- 535 Casey B J, Giedd J N, Thomas K M 2000. Structural and functional brain development and its relation to  
536 cognitive development. *Biological Psychology* 54:241–257.
- 537 Cole M W, Ito T, Bassett D S, Schultz D H 2016. Activity flow over resting-state networks shapes cognitive  
538 task activations. *Nature Neuroscience* 19:1718–1726.
- 539 Combrisson E, Vallat R, O'Reilly C, Jas M, Pasquarella A, l Saive A, Thiery T, Meunier D, Altukhov D,  
540 Lajnef T, Ruby P, Guillot A, Jerbi K 2019. Visbrain: a multi-purpose GPU-accelerated open-source suite  
541 for multimodal brain data visualization. *Frontiers in Neuroinformatics* 13:1–14.

- 542 Crone N. E., Korzeniewska A., Franaszczuk P.J. 2011. Cortical gamma responses: searching high and  
543 low. International Journal of Psychophysiology 79:9–15.
- 544 Ezzyat Y, Kragel J E, Burke J F, Levy D F, Lyalenko A, Wanda P, O'Sullivan L, Hurley K B, Busyggin S,  
545 Pedisich I, Sperling M R, Worrell G A, Kucewicz M T, Davis K A, Lucas T H, Inman C S, Lega B C, Jobst  
546 B C, Sheth S A, Zaghloul K, Jutras M J, Stein J M, Das S R, Gorniak R, Rizzuto D S, Kahana M J 2017.  
547 Direct brain stimulation modulates encoding states and memory performance in humans. Current  
548 Biology 27:1–8.
- 549 Ezzyat Y, Wanda P A, Levy D F, Kadel A, Aka A, Pedisich I, Sperling M R, Sharan A D, Lega B C,  
550 Burks A, Gross R E, Inman C S, Jobst B C, Gorenstein M A, Davis K A, Worrell G A, Kucewicz  
551 M T, Stein J M, Gorniak R, Das S R, Rizzuto D S, Kahana M J 2018. Closed-loop stimulation  
552 of temporal cortex rescues functional networks and improves memory. Nature Communications  
553 9: <https://doi.org/10.1038/s41467-017-02753-0>.
- 554 Feingold J, Gibson D J, DePasquale B, Graybiel A M 2015. Bursts of beta oscillation differentiate postperfor-  
555 mance activity in the striatum and motor cortex of monkeys performing movement tasks. Proceedings  
556 of the National Academy of Science USA 112:13687–13692.
- 557 Finn E S, Shen X, Scheinost D, Rosenberg M D, Huang J, Chun M M, Papademetris X, Constable R T 2015.  
558 Functional connectome fingerprinting: identifying individuals using patterns of brain connectivity.  
559 Nature Neuroscience 18:1664 – 1671.
- 560 Fries P., Nikolić D., Singer W. 2007. The gamma cycle. Trends in Neurosciences 30:309–316.
- 561 Goñi J, van den Heuvel M P, Avena-Koenigsberger A, de Mendizabal N V, Betzel R F, Griffa A, Hagmann  
562 P, Corominas-Murtra B, Thiran J-P, Sporns O 2014. Resting-brain functional connectivity predicted  
563 by analytic measures of network communication. Proceedings of the National Academy of Sciences  
564 111:833–838.

- 565 Grabner G., Janke A. L., Budge M. M., Smith D., Pruessner J., Collins D. L. 2006. Symmetric atlasing  
566 and model based segmentation: an application to the hippocampus in older adults. *Medical Image  
567 Computing and Computer-Assistend Intervention* 9:58–66.
- 568 Haxby J. V., Gobbini M. I., Furey M. L., Ishai A., Schouten J. L., Pietrini P. 2001. Distributed and  
569 overlapping representations of faces and objects in ventral temporal cortex. *Science* 293:2425–2430.
- 570 Haxby J V, Guntupalli J S, Connolly A C, Halchenko Y O, Conroy B R, Gobbini M I, Hanke M, Ramadge  
571 PJ 2011. A common, high-dimensional model of the representational space in human ventral temporal  
572 cortex. *Neuron* 72:404–416.
- 573 Hillebrand A, Singh K D, Holliday I E, Furlong P L, Barnes G R 2005. A new approach to neuroimaging  
574 with magnetoencephalography. *Human Brain Mapping* 25:199–211.
- 575 Honey C J, Sporns O, Cammoun L, Gigandet X, Thiran J P, Meuli R, Hagmann P 2009. Predicting  
576 human resting-state functional connectivity from structural connectivity. *Proceedings of the National  
577 Academy of Science USA* 106:2035–2040.
- 578 Honey C. J., Thesen T., Donner T. H., Silbert L. J., Carlson C. E., Devinsky O., Doyle J. C., Rubin N.,  
579 Heeger D. J., Hasson U. 2012. Slow cortical dynamics and the accumulation of information over long  
580 timescales. *Neuron* 76:423–434.
- 581 Horak P C, Meisenhelter S, Song Y, Testorf M E, Kahana M J, Viles W D, Bujarski K A, Connolly A C,  
582 Robbins A A, Sperling M R, Sharan A D, Worrell G A, Miller L R, Gross R E, Davis K A, Roberts D W,  
583 Lega B, Sheth S A, Zaghloul K A, Stein J M, Das S R, Rizzuto D S, Jobst B C 2017. Interictal epileptiform  
584 discharges impair word recall in multiple brain areas. *Epilepsia* 58:373–380.
- 585 Huster R J, Debener S, Eichele T, Herrmann C S 2012. Methods for simultaneous EEG-fMRI: an intro-  
586 ductory review. *The Journal of Neuroscience* 32:6053–6060.

- 587 Ihara A, Hirata M, Yanagihara K, Ninomiya H, Imai K, Ishii R, Osaki Y, Sakihara K, Izumi H, Imaoka  
588 H, Kato A, Yoshimine T 2003. Neuromagnetic gamma-band activity in the primary and secondary  
589 somatosensory areas. *NeuroReport* 14:273–277.
- 590 Jacobs J., Manning J.R., Kahana M.J. 2010. Response to Miller: “Broadband” vs. “high gamma” electro-  
591 corticographic signals. *Journal of Neuroscience* 30.
- 592 Jahanshad N, Kochunov P V, Sprooten E, Mandl R C, Nichols T E, Almasy L, Blangero J, Brouwer R M,  
593 Curran J E, de Zubicaray G I, Duggirala R, Fox P T, Hong L E, Landman B A, Martin N G, McMahon  
594 K L, Medland S E, Mitchell B D, Olvera R L, Peterson C P, Starr J M, Sussmann J E, Toga A W, Wardlaw  
595 J M, Wright M J, Pol H E Hulshoff, Pastin M E, McIntosh A M, Deary I J, Thompson P M, Glahn D C  
596 2013. Multi-site genetic analysis of diffusion images and voxelwise heritability analysis: A pilot project  
597 of the enigma-dti working group. *NeuroImage* 81:455–469.
- 598 Jurkiewicz M T, Gaetz W C, Bostan A C, Cheyne D 2006. Post-movement beta rebound is generated in  
599 motor cortex: Evidence from neuromagnetic recordings. *NeuroImage* 32:1281–1289.
- 600 Kragel J E, Ezzyat Y, Sperling M R, Gorniak R, Worrell G A, Berry B M, Inman C, Lin J-J, Davis K A, Das  
601 S R, Stein J M, Jobst B C, Zaghloul K A, Sheth S A, Rizzuto D S, Kahana M J 2017. Similar patterns of  
602 neural activity predict memory formation during encoding and retrieval. *NeuroImage* 155:70–71.
- 603 Kucewicz M T, Berry B M, Kremen V, Brinkmann B H, Sperling M R, Jobst B C, Gross R E, Lega B, Sheth  
604 S A, Stein J M, Das S R, Gorniak R, Stead S M, Rizzuto D S, Kahana M J, Worrell G A 2017. Dissecting  
605 gamma frequency activity during human memory processing. *Brain* 140:1337–1350.
- 606 Kucewicz M T, Berry B M, Miller L R, Khadjevand F, Ezzyat Y, Stein J M, Kremen V, Brinkmann B H,  
607 Wanda P, Sperling M R, Gorniak R, Davis K A, Jobst B C, Gross R E, Lega B, Gompel J Van, Stead S M,  
608 Rizzuto D S, Kahana M J, Worrell G A 2018. Evidence for verbal memory enhancement with electrical  
609 brain stimulation in the lateral temporal cortex. *Brain* 141:971–978.

- 610 Kucyi A, Schrouff J, Bickel S, Foster B L, Shine J M, Parvizi J 2018. Intracranial electrophysiology reveals  
611 reproducible intrinsic functional connectivity with human brain networks. *Journal of Neuroscience*  
612 38:4230–4242.
- 613 Lin J-J, Rugg M D, Das S, Stein J, Rizzuto D S, Kahana M J, Lega B C 2017. Theta band power increases in  
614 the posterior hippocampus predict successful episodic memory encoding in humans. *Hippocampus*  
615 27:1040–1053.
- 616 Manning J. R., Jacobs J., Fried I., Kahana M. J. 2009. Broadband shifts in LFP power spectra are correlated  
617 with single-neuron spiking in humans. *The Journal of Neuroscience* 29:13613–13620.
- 618 Manning J. R., Polyn S. M., Baltuch G., Litt B., Kahana M. J. 2011. Oscillatory patterns in temporal  
619 lobe reveal context reinstatement during memory search. *Proceedings of the National Academy of  
620 Sciences, USA* 108:12893–12897.
- 621 Manning J R, Ranganath R, Norman K A, Blei D M 2014. Topographic factor analysis: a Bayesian model  
622 for inferring brain networks from neural data. *PLoS One* 9:e94914.
- 623 Manning J. R., Sperling M. R., Sharan A., Rosenberg E. A., Kahana M. J. 2012. Spontaneously reactivated  
624 patterns in frontal and temporal lobe predict semantic clustering during memory search. *The Journal  
625 of Neuroscience* 32:8871–8878.
- 626 Manning J R, Zhu X, Willke T L, Ranganath R, Stachenfeld K, Hasson U, Blei D M, Norman K A  
627 2018. A probabilistic approach to discovering dynamic full-brain functional connectivity patterns.  
628 *NeuroImage* 180:243–252.
- 629 Matsumoto Joseph Y, Stead Matt, Kucewicz Michal T, Matsumoto Andrew J, Peters Pierce A, Brinkmann  
630 Benjamin H, Danstrom Jane C, Goerss Stephan J, Marsh W Richard, Meyer Fred B et al. 2013. Network  
631 oscillations modulate interictal epileptiform spike rate during human memory. *Brain* 136.

- 632 Miller K. J., Leuthardt E. C., Schalk G., Rao R. P. N., Anderson N. R., Moran D. W., Miller J. W.,  
633 Ojemann J. G. 2007. Spectral changes in cortical surface potentials during motor movement. *Journal*  
634 of Neuroscience 27:2424–2432.
- 635 Miller K. J., Shenoy P., den Nijs M., Sorensen L. B., Rao R. P. N., Ojemann J. G. 2008. Beyond the gamma  
636 band: the role of high-frequency features in movement classification. *IEEE Transactions on Biomedical*  
637 *Engineering* 55:1634 – 1637.
- 638 Mori S, Oishi K, Jiang H, Jiang L, Li X, Akhter K, Hua K, Faria A V, Mahmood A, Woods R, Toga A W,  
639 Pike G B, Neto P R, Evans A, Zhang J, Huang H, Miller M I, van Zijl P, Mazziotta J 2008. Stereotaxic  
640 white matter atlas based on diffusion tensor imaging in an icbm template. *NeuroImage* 40:570–582.
- 641 Norman K. A., Newman E., Detre G., Polyn S. M. 2006. How inhibitory oscillations can train neural  
642 networks and punish competitors. *Neural Computation* 18:1577–1610.
- 643 Owen L L W, Chang T H, Manning J R 2019. High-level cognition during story listening is reflected in  
644 high-order dynamic correlations in neural activity patterns. *bioRxiv* doi.org/10.1101/763821.
- 645 Rasmussen C E 2006. Gaussian processes for machine learning. MIT Press.
- 646 Reddy P G, Betzel R F, Khambhati A N, Shah P, Kini L, Litt B, Lucas T H, Davis K A, Bassett D S 2018. Ge-  
647 netic and neuroanatomical support for functional brain network dynamics in epilepsy authors genetic  
648 and neuroanatomical support for functional brain network dynamics in epilepsy. *arXiv* 1809.03934.
- 649 Rubin T N, Kyoejo O, Gorgolewski K J, Jones M N, Poldrack R A, Yarkoni T 2017. Decoding brain activity  
650 using a large-scale probabilistic functional-anatomical atlas of human cognition. *PLoS Computational*  
651 *Biology* 13:e1005649.
- 652 Sarvas J 1987. Basic mathematical and electromagnetic concepts of the biomagnetic inverse problem.  
653 *Phys. Med. Biol.* 32:11–22.

- 654 Sawyer Robert J 1995. *The Terminal Experiment*. HarperPrism.
- 655 Scangos K W, Khambhati A N, Daly P M, Owen L L W, Manning J R, Ambrose J B, Austin E, Dawes  
656 H E, Krystal A D, Chang E F 2020. Biomarkers of depression symptoms defined by direct intracranial  
657 neurophysiology. *bioRxiv* doi.org/10.1101/2020.02.14.943118.
- 658 Sederberg P. B., Kahana M. J., Howard M. W., Donner E. J., Madsen J. R. 2003. Theta and gamma  
659 oscillations during encoding predict subsequent recall. *Journal of Neuroscience* 23:10809–10814.
- 660 Sederberg P. B., Schulze-Bonhage A., Madsen J. R., Bromfield E. B., Litt B., Brandt A., Kahana M. J. 2007a.  
661 Gamma oscillations distinguish true from false memories. *Psychological Science* 18:927–932.
- 662 Sederberg P. B., Schulze-Bonhage A., Madsen J. R., Bromfield E. B., McCarthy D. C., Brandt A., Tully M. S.,  
663 Kahana M. J. 2007b. Hippocampal and neocortical gamma oscillations predict memory formation in  
664 humans. *Cerebral Cortex* 17:1190–1196.
- 665 Sejnowski T J, Churchland P S, Movshon J A 2014. Putting big data to good use in neuroscience. *Nature  
666 Neuroscience* 17:1440–1441.
- 667 Sherman M A, Lee S, Law R, Haegens S, Thorn C A, Hämäläinen M S, Moore C I, Jones S R 2016. Neural  
668 mechanisms of transient neocortical beta rhythms: Converging evidence from humans, computational  
669 modeling, monkeys, and mice. *Proceedings of the National Academy of Science USA* 113:E4885–E4894.
- 670 Simony E, Honey C J, Chen J, Hasson U 2016. Uncovering stimulus-locked network dynamics during  
671 narrative comprehension. *Nature Communications* 7:1–13.
- 672 Snyder A Z 1991. Dipole source localization in the study of EP generators: a critique. *Electroencephalog-  
673 raphy and Clinical Neurophysiology* 80:321–325.
- 674 Solomon E A, Gross R, Lega B, Sperling M R, Worrell G, Sheth S A, Zaghloul K A, Jobst B C, Stein J M, Das  
675 S, Gorniak R, Inman C, Seger S, Kragel J E, Rizzuto D S, Kahana M J 2018. Mtl functional connectivity  
676 predicts stimulation-induced theta power. *Nature Communications* In press.

- 677 Sporns O, Betzel R F 2016. Modular brain networks. *Annual Review of Psychology* 67:613–640.
- 678 Talairach J., Tournoux P. 1988. Co-planar stereotaxic atlas of the human brain. Verlag, Stuttgart.
- 679 Tavor I, Jones O Parker, Mars R B, Smith S M, Behrens T E, Jbabdi S 2016. Task-free MRI predicts  
680 individual differences in brain activity during task performance. *Science* 352:216–220.
- 681 Tomasi D, Volkow N D 2011. Association between functional connectivity hubs and brain networks.  
682 *Cerebral Cortex* 21:2003–2013.
- 683 Turk-Browne N B 2013. Functional interactions as big data in the human brain. *Science* 342:580–584.
- 684 Weidemann C T, Kragel J E, Lega B C, Worrell G A, Sperling M R, Sharan A D, Jobst B C, Khadjevand F,  
685 Davis K A, Wanda P A, Kadel A, Rizzuto D S, Kahana M J 2019. Neural activity reveals interactions  
686 between episodic and semantic memory systems during retrieval. *Journal of Experimental Psychology:  
687 General* 148:1–12.
- 688 Wu H C, Nagasawa T, Brown E C, Juhasz C, Rothermel R, Hoechstetter K, Shah A, Mittal S, Fuerst D, Sood  
689 S, Asano E 2011. Gamma-oscillations modulated by picture naming and word reading: Intracranial  
690 recording in epileptic patients. *Clinical Neurophysiology* 122:1929–1942.
- 691 Yeo B T T, Krienen F M, Sepulcre J, Sabuncu M R, Lashkari D, Hollinshead M, Roffman J L, Smoller J W,  
692 Zollei L, Polimieni J R, Fischl B, Liu H, Buckner R L 2011. The organization of the human cerebral  
693 cortex estimated by intrinsic functional connectivity. *Journal of Neurophysiology* 106:1125–1165.
- 694 Zalesky A, Fornito A, Harding I H, Cocchi L, Yücel M, Pantelis C, Bullmore E T 2010. Whole-brain  
695 anatomical networks: does the choice of nodes matter? *NeuroImage* 50:970–983.